Magnetophotoluminescence in GaAs/AlAs core-multishell nanowires: A theoretical investigation

Fabrizio Buscemi,[1,][*] Miquel Royo,[2,3] Andrea Bertoni,[3] and Guido Goldoni[1,3]

[1]*Department of Physics, Informatics, and Mathematics, University of Modena and Reggio Emilia, Via Campi 213/A, I-41125 Modena, Italy*
[2]*Departament de Quimíca Física i Analítica, Universitat Jaume I, E-12080 Castelló, Spain*
[3]*Consiglio Nazionale delle Ricerche NANO S3, Institute for Nanoscience, Via Campi 213/A, I-41125 Modena, Italy*

The magnetophotoluminescence in modulation doped core-multishell nanowires is predicted as a function of photoexcitation intensity in nonperturbative transverse magnetic fields. We use a self-consistent field approach within the effective mass approximation to determine the photoexcited electron and hole populations, including the complex composition and anisotropic geometry of the nanomaterial. The evolution of the photoluminescence is analyzed as a function of (i) photoexcitation power, (ii) magnetic field intensity, (iii) type of doping, and (iv) anisotropy with respect to field orientation.

PACS number(s): 73.21.Hb, 73.43.Cd, 73.63.Nm, 75.75.−c

I. INTRODUCTION

In the last decade, semiconductor nanowires (NWs) have received increasing attention owing to their potential applications in nanotechnology [1]. They represent promising candidates for a wide range of novel ultrafast electronic and optoelectronic nanodevices including high electron mobility transistors [2], photovoltaic cells [3], single-photon emitters [4], and lasers [5]. Critical steps have been taken in these directions in the last years. Long single-crystal defect-free cores [6,7], selective radial doping [8], and lateral overgrowth with high-quality interfaces [9] have been successfully realized. Most importantly, complex radial modulation doped heterostructures are now being engineered in core-multishell NWs [10–13]. More complex than their planar counterparts, radial heterostructures in these systems may host high-mobility electron/hole gases with an inhomogeneous localization in the section of the NW, which strongly depends on doping density and gate potentials [14–16].

Magnetic states of such axial electron gases have been investigated in cylindrical systems [17–19] or in wrapped heterojunctions with prismatic symmetry [20–22]. In the quantum Hall regime, the magnetic field competes with the self-consistent confinement field. Recent self-consistent field calculations of realistic GaAs/AlGaAs core-shell NWs in transverse fields [21] showed that at high carrier density the carrier-carrier repulsion results in complex magnetic bands, corresponding to inhomogeneous charge localization at the prismatic heterointerfaces of the nanomaterial.

Intraband optical spectroscopy is a key component in the investigation of properties of single semiconductor NWs and NW heterostructures [11–13,23–26]. In particular, photoluminescence (PL) has been successfully used in bare and core-multishell (CMS) NWs in order to analyze the dynamics of photoexcited electron-hole plasmas [23–25] and the quantum confinement effects [11–13]. Magneto-PL in GaAs/AlAs CMS NWs has been applied to undoped [27] and doped samples [12], where the magnetic field dependence of peaks ascribed to confined carrier emission has been examined.

In this work, we consider magneto-PL in modulation doped GaAs/AlAs CMS NWs with an inversion or an accumulation layer at the inner GaAs/AlAs heterointerface in a transverse magnetic field. Using a self-consistent envelope-function approach, we predict the magneto-PL at different excitation powers and identify nonlinear effects due to filling and restructuring of the free-carrier gas. Furthermore, we investigate the effects of the type of doping and of the structure anisotropy on the magneto-PL.

The paper is organized as follows. In Sec. II, we describe the physical and numerical modeling of the modulation doped CMS NW used to evaluate the hole and electron states and from these the PL spectra. The results obtained from our numerical calculations are discussed in Sec. III. First, the prototype nanostructure under investigation and its relevant physical parameters are presented in Sec. III A. Then, Sec. III B illustrates predictions for the *p*- and *n*-doped system at various regimes of photoexcitation power. Anisotropy with respect to field orientation is examined in Sec. III C. We summarize our results in Sec. IV.

II. THEORETICAL APPROACH

Electron and hole states are determined by a self-consistent Schrödinger-Poisson approach [14,15,21]. Within a single parabolic band effective-mass approximation, the Hamiltonians for holes (*h*, upper sign) and electrons (*e*, lower sign) in an external magnetic field [28] are given by

$$\left[(\mathbf{P} \mp q\mathbf{A}(\mathbf{R})) \frac{1}{2m^*_{h(e)}(\mathbf{R})} (\mathbf{P} \mp q\mathbf{A}(\mathbf{R})) \mp E_{V(C)}(\mathbf{R}) \pm qV(\mathbf{R}) \right],$$
(1)

respectively, where $\mathbf{R}=(x,y,z)$ represents a three-dimensional (3D) coordinate, $\mathbf{P}$ is the conjugate momentum operator, q is the positive unit charge, $\mathbf{A}(\mathbf{R})$ is the magnetic vector potential, $m^*_{e(h)}(\mathbf{R})$ is the material-dependent effective mass of electrons (holes), and $E_V(\mathbf{R})$, $E_C(\mathbf{R})$, and $V(\mathbf{R})$ are the local valence-band edge, the local conduction-band edge, and the electrostatic potential generated by the free carriers and the dopants, respectively. Electron-hole interactions are taken into account within a mean-field approximation through the self-consistent potential $V(\mathbf{R})$, i.e., "excitonic"

[*]fabrizio.buscemi@unimore.it

effects are not included in our calculations, as they are expected to be negligible at densities larger than $\approx 10^6$ electron/cm [29–31].

The transverse magnetic field is described in the Landau gauge $\mathbf{A}(\mathbf{R}) = B(y \cos\theta - x \sin\theta)\hat{z}$, where θ denotes the angle between the field and the x axis (see Fig. 1). We shall consider two possible orientations of the field:

(i) perpendicular to the facets ($\theta = \pi/2$) and (ii) along the maximal diameter ($\theta = \pi/3$).

Since the field does not break the translational invariance, the 3D wave functions can be factorized as $\Psi_n^{e(h)}(\mathbf{R}) = e^{ikz}\psi_{n,k}^{e(h)}(\mathbf{r})$, where $\mathbf{r} = (x,y)$ and k is the wave vector along the nanowire axis. Then the two-dimensional (2D) wave functions $\psi_{n,k}^{e(h)}(\mathbf{r})$ are solutions of the Schrödinger equations

$$
\left[-\frac{\hbar^2}{2}\nabla_{\mathbf{r}}\frac{1}{m_{h,\perp}^*(\mathbf{r})}\nabla_{\mathbf{r}} + \frac{1}{2}m_{h,\|}^*(\mathbf{r})\omega_{c,h}^2(\mathbf{r})\left(y\cos\theta - x\sin\theta - kl_B^2\right)^2 - E_V(\mathbf{r}) + qV(\mathbf{r}) \right]\psi_{n,k}^h(\mathbf{r}) = -E_{n,k}^h\psi_{n,k}^h(\mathbf{r}),
$$
$$
\left[-\frac{\hbar^2}{2}\nabla_{\mathbf{r}}\frac{1}{m_e^*(\mathbf{r})}\nabla_{\mathbf{r}} + \frac{1}{2}m_e^*(\mathbf{r})\omega_{c,e}^2(\mathbf{r})\left(y\cos\theta - x\sin\theta + kl_B^2\right)^2 + E_C(\mathbf{r}) - qV(\mathbf{r}) \right]\psi_{n,k}^e(\mathbf{r}) = E_{n,k}^e\psi_{n,k}^e(\mathbf{r}),
$$

$$(2)$$

where $\omega_{c,e(h)}(\mathbf{r}) = qB/m_{e(h,\|)}^*(\mathbf{r})$ is the hole (electron) cyclotron frequency, $l_B = \sqrt{\hbar/(qB)}$ is the magnetic length, and $E_{n,k}^{h(e)}$ is the energy of the hole (electron) state. Note that we distinguish between the hole effective mass in the section of the CMS NW, $m_{h,\perp}^*$, and the hole effective mass along the wire, $m_{h,\|}^*$, to take into consideration the strong mass anisotropy of GaAs. The electron effective mass, m_e^*, is assumed to be isotropic.

Similarly to the familiar case of a planar Hall bar, in the above equations the effect of the magnetic field is represented by an harmonic potential displaced by kl_B^2 from the nanowire axis. Therefore, in general, $E_{n,k}^{h(e)}$ is not parabolic in k at large magnetic fields. Note that Eqs. (2) are coupled by the electrostatic field $V(\mathbf{r})$ which is determined by both electron and hole densities, as shown below.

Equations (2) are numerically solved by the box integration method on a triangular grid with hexagonal elements [15,21]. At each magnetic field the equations are solved on a grid of wave vectors in $[0,k_{\max}]$ [32]. The k domain is discretized in steps $\Delta k = 0.075$ nm^{-1}, while $k_{\max}$ is taken sufficiently larger than the Fermi-wave vector that its occupation is negligible.
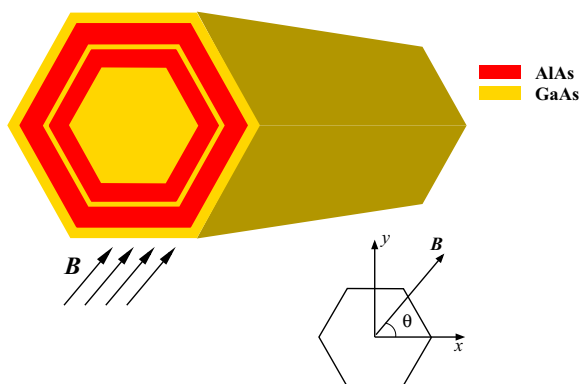

FIG. 1. (Color online) Sketch of the GaAs/AlAs core-multishell NW investigated in this work. The GaAs core is overgrown with AlAs/GaAs/AlAs layers forming a narrow quantum well and a GaAs capping layer. The GaAs quantum well serves as a doping layer with a homogeneously distributed density of donors or acceptors n_D or n_A), respectively. The transverse magnetic field forms an angle θ with the x axis.

The hole and electron densities are evaluated at temperature T from

$$
n_h^\circ(\mathbf{r}, E_F) = 2\sum_n \int_{-k_{\max}}^{k_{\max}} \frac{dk}{2\pi} |\psi_{n,k}^h(\mathbf{r})|^2 f\left(\frac{-E_{n,k}^h + E_F}{k_B T}\right),
$$
$$
n_e^\circ(\mathbf{r}, E_F) = 2\sum_n \int_{-k_{\max}}^{k_{\max}} \frac{dk}{2\pi} |\psi_{n,k}^e(\mathbf{r})|^2 f\left(\frac{E_{n,k}^e - E_F}{k_B T}\right),
$$

$$(3)$$

where the factor 2 accounts for spin degeneracy, and $f(x) = 1/(1 + e^x)$ is the Fermi function. E_F indicates the Fermi level which is determined by surface states and, therefore, by the type of doping. The charge densities in Eqs. (3) depend on the fully ionized dopants, i.e., photoexcited carriers are not included here. As shown elsewhere [15,21], the symmetry and localization of n_h° and n_e° are strongly influenced by the level of doping, due to competing energy scales [12,21]. The linear free charge density per unit length provided by the dopants $n_{1,e(h)}^\circ$ can finally be calculated from

$$
n_{1,e(h)}^\circ = \int_A n_{e(h)}^\circ(\mathbf{r}, E_F)d\mathbf{r}. \tag{4}
$$

Its dependence from E_F is omitted for brevity.

The laser field also excites electron-hole pairs with a linear density n_l^{ph}. If the photoexcited density is not negligible with respect to the free charge induced by dopants, the self-consistent field should take these charges into account. The total electron (hole) linear density $n_{1,e(h)}$ is

$$
n_{1,e(h)} = n_{1,e(h)}^\circ + n_l^{\mathrm{ph}}. \tag{5}
$$

In order take into account the photoexcited charge, we shift the Fermi level E_F to $E_F^{e(h)}$ (in general $E_F^h \neq E_F^e$) until

$$
\int_A n_{e(h)}\left(\mathbf{r}, E_F^{e(h)}\right)d\mathbf{r} - n_{1,e(h)} = 0. \tag{6}
$$

This amounts to the charge neutrality condition in an undoped sample. In practice, we obtain $E_F^{e(h)}$ from Eqs. (3)–(6) by means of the bisection method.

Once the total electron and hole densities are computed, the electrostatic potential $V(\mathbf{r})$ is obtained by solving the Poisson

equation

$$\nabla_{\mathbf{r}}[\epsilon_r(\mathbf{r})\nabla_{\mathbf{r}}V(\mathbf{r})] = -\frac{q}{\epsilon_0}[n_h(\mathbf{r}) - n_e(\mathbf{r}) + n_D(\mathbf{r}) - n_A(\mathbf{r})],$$

$$(7)$$

where $\epsilon_r(\mathbf{r})$ and ϵ_0 describe the position-dependent dielectric constant and the vacuum permittivity, while $n_{D(A)}(\mathbf{r})$ denotes the ionized donor (acceptor) density. Dirichlet boundary conditions are used to solve Eq. (7) with the potential on the domain boundaries set to zero.

The electrostatic potential is inserted into Eqs. (2) and the whole procedure is iterated until self-consistency is achieved, that is, the relative variation of both the electron and hole density is <0.01 at each point of the simulation domain.

The PL spectra is computed under the assumption that carriers are thermalized in the lowest electronic levels by fast nonradiative processes. Thus, the intensity of the PL signal is given by [33]

$$I_{\text{PL}}(\omega) \propto \sum_{n,m} \int_{-k_{\max}}^{k_{\max}} \frac{dk}{2\pi} \left|\langle\psi_{n,k}^e|\psi_{m,k}^h\rangle\right|^2$$

$$\times f\left(\frac{-E_{m,k}^h + E_F^h}{k\text{T}}\right) f\left(\frac{E_{n,k}^e - E_F^e}{k\text{T}}\right)$$

$$\times \Im\left[\frac{1}{E_{n,k}^e - E_{m,k}^h - \hbar\omega - i\gamma}\right],$$

where $\langle\psi_{n,k}^e|\psi_{m,k}^h\rangle = \int d\mathbf{r}\,\psi_{n,k}^{e*}(\mathbf{r})\psi_{m,k}^h(\mathbf{r})$, the product of the two Fermi distributions describes the occupation of the states involved in the photoemission, and the last term accounts for a Lorentzian broadening of the peaks due to incoherent processes by means of a phenomenological parameter γ. As usual for interband transitions at optical frequencies, only *vertical* transitions are taken into account.

III. RESULTS

A. Structure details

We simulate a prototype NW with the same compositional parameters as in Ref. [12]. A GaAs core of diameter 60 nm (facet to facet) is surrounded by a 3-nm/1-nm/3-nm AlAs/GaAs/AlAs multilayer and a 13-nm GaAs capping layer. Donors or acceptors are uniformly distributed in the narrow GaAs quantum well (QW). For p doping we assume a Fermi level pining at 400 meV above the valence-band edge [34], while for n doping we assume midgap pinning. The PL phenomenological linewidth $\gamma = 0.5$ meV and all calculations have been performed at temperature T = 1.8 K.

Material parameters are reported in Table I. Hole masses are chosen as those of a planar quantum well grown along the [110] direction, which corresponds to the radial QW of the CMS NW structure. Appropriate expressions of the effective masses along the quantization axis [110] of the quantum well and the in-plane direction (here corresponding to the in-wire direction [111]) are obtained, e.g., in Ref. [36] from the diagonalization of the Luttinger Hamiltonian. Note that the "heavy" mass along the [110] direction is taken as isotropic in the section of the CMS NW, which is why a much lighter mass describes the heavy hole dispersion along the wire.

TABLE I. Material parameters used in the numerical calculations [35]. The relative effective masses in the axial (z) and transverse (**r**) directions are given in units of the free-electron mass.

	GaAs	AlAs
$E_C - E_V$(meV)	1519	3020
m_e^*	0.062	0.19
$m_{h,\parallel}^*$	0.082	0.109
$m_{h,\perp}^*$	0.680	0.818

Note that in our procedure we do not include light-hole states. We have checked that light-hole sub-bands (evaluated within a parabolic approximation with the light-hole mass in the [110] growth direction [36]) lie well below the Fermi level. Clearly, light-hole states might still contribute to heavy-hole states via spin-orbit coupling, which is neglected in the parabolic approximation assumed in this work. Unfortunately, spin-orbit coupled states have not been investigated for realistic models of CMS NWs. However, from previous calculations in semiconductor quantum wires, we may expect these effects to be small for these weakly confined states [37].

Note that the narrow GaAs QW acts here as a doping layer. Due to its narrow thickness, no quantum state is hosted by the QW itself, and all free charge accumulates in an inversion or accumulation layer, depending on the type of doping, in the core or at the inner heterointerface, as we shall discuss below.

B. Fan diagrams

We examine the evolution of the magneto-PL with a transverse magnetic field for p- and n-doped samples. We shall consider three levels of the photoexcited charge, namely, negligible, lower, and comparable to the free charge density induced by a typical doping level.

1. p doping

We first consider a p-doped sample with $n_A = 2.5 \times 10^{19}\text{cm}^{-3}$, which corresponds to a linear free hole density $n_{1,h}^{\circ} = 8.5 \times 10^6\text{cm}^{-1}$. We first consider a low excitation density $n_1^{\text{ph}} = 10^5\text{cm}^{-1} \ll n_{1,h}^{\circ}$.

In Fig. 2, left panel, we show the dispersion of the magnetic levels for holes and electrons evaluated at selected B values. The evolution of the magnetic sub-bands for conduction electrons resembles that of Landau levels and edge states in planar Hall bars [38]. Indeed, as shown in the inset, the electron charge is localized in the core, since n_l^{ph} is very small and it is not able to bend the conduction edge. Therefore, electron states are similar to those of a QW in a vertical field, here represented by the NW core, and bend up at increasing k, which correspond to edge states confined by the field on the lateral boundaries of the GaAs core [21].

This is in contrast with the dispersion of holes, which becomes flat at lower fields and develops nonmonotonous behavior at large k. Such a behavior is not due to the strong anisotropy of the hole mass but to the emergence of peculiar localized states [18]. Indeed, holes, which here are mainly generated by doping so that $n_{l,h} \gg n_{l,e}$, create an accumulation layer near the heterointerface, with an approximately tubular
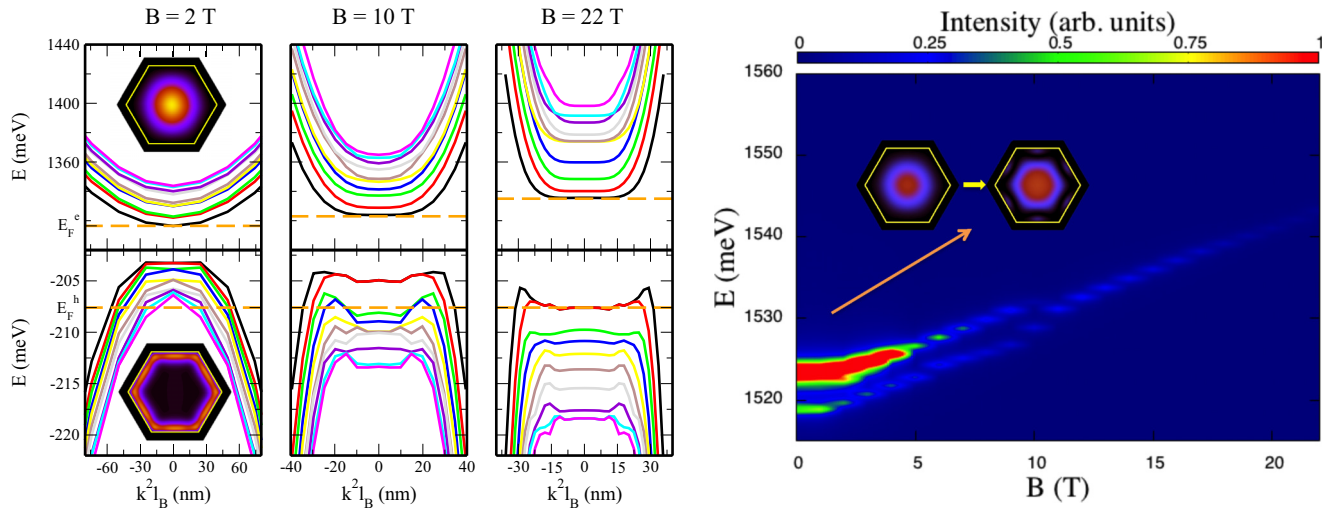
FIG. 2. (Color online) Magnetic states and magneto-PL calculated for $n_A = 2.5 \times 10^{19}$ cm^{-3} and $n_1^{Ph} = 10^5$ cm^{-1}. Here B is normal to the facets ($\theta = \pi/2$). Left: Electron (top) and hole (bottom) sub-bands vs kl_B^2 at selected fields B as indicated. The horizontal lines indicate the energy of the electron/hole Fermi level. The hexagonal insets show the electron (top) and hole (bottom) charge density at $B = 2$ T. Right: Calculated PL spectra. The inset displays the squared envelope functions for the electron (left) and hole (right) state whose recombination yields the strong peak at $E = 1523$ meV when $B = 0$. The regular intensity oscillations are a graphic artifact due to the course magnetic field grid.

geometry, as shown in the inset. As discussed in Ref. [18], at sufficiently large fields the energy dispersion curves develop minima which correspond to states localized at the flanks of the tube, where the vertical component of the field with respect to the charge layer (and the associated confinement energy) is vanishing. Note from Fig. 2 (left) that several hole levels are occupied, while electrons only occupy the lowest magnetic sub-band. The number of occupied sub-bands in the hole states decrease with increasing field. At intermediate fields ($B = 10$ T), only four hole sub-bands are occupied and at 22 T only two hole magnetic sub-bands lie below or close to the hole Fermi level.

The evolution of the ground state $n = 1$ and $k = 0$ for electrons and holes is shown in Fig. 3 at selected magnetic field intensities. While the electron state is delocalized over the core, the hole state is localized at the top and bottom of the
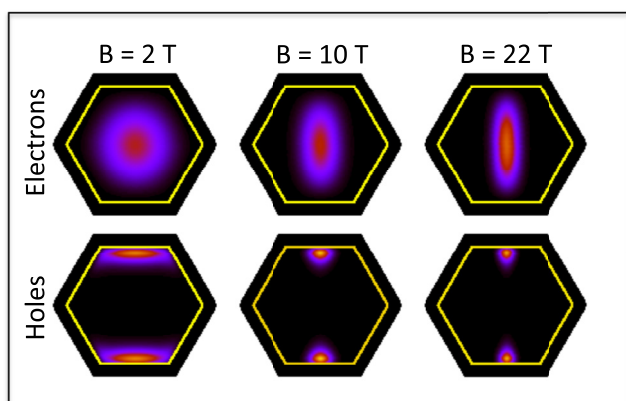

FIG. 3. (Color online) Square modulus of the lowest $k = 0$ electron (top) and hole (bottom) envelope function at selected fields, as indicated, for the sample of Fig. 2.

structure (here the field is in the vertical direction). Clearly, the states extend laterally by about l_B.

The evolution of the calculated PL spectra with field is shown in the fan diagrams of Fig. 2, right panel. At zero field, the spectrum exhibits two peaks. The lowest in energy, close to the band gap of bulk GaAs at 1519 meV, is due to the electron and hole (e-h) ground state, coupling the states shown in Fig. 3. Due to the small overlap, this peak is weak. The second, much stronger, peak originates from the recombination of the electron ground state and the hole lowest excited state spreading over the center of the GaAs core, hence the large oscillator strength (see the inset in the right panel of Fig. 2).

In the PL spectra in Fig. 2 we can distinguish two different field regimes. At low fields, the peaks undergo a quadratic diamagnetic shift and progressively reduce their intensity. The stronger peak disappears at $B \sim 10$ T, due to the decreasing occupation of the hole excited state ($n = 3$). Indeed, even though the global hole density is almost independent from B, as the field increases the sub-bands flatten and accommodate a larger number of carriers in the lowest sub-band with $k \neq 0$ as shown in Fig. 2 (left). This leads to a rearrangement of the hole gas and the lowest-energy sub-bands and, in turn, the appearance of a kink in the emission line of the ground e-h state in the region around $B \sim 10$ T. As shown in Fig. 4, just at the complete depletion of the $n = 3$ hole level the gas redistribution affects the energy of the ground hole state at $k = 0$ which increases by ~4 meV. Such an effect is related to the Fermi-level pinning, that is, E_F^h goes from being pinned at the $n = 3$ sub-band to the flat $n = 1, 2$ ones as found in other works [21]. Note that in the present calculation PL spectra originate from the recombination of the hole and electron states with $k = 0$, since this is the only occupied state in the conduction band. At larger fields, when the dispersion flattens, also finite wave vectors are occupied. However, such states are localized on opposite sides of the structures for electrons and
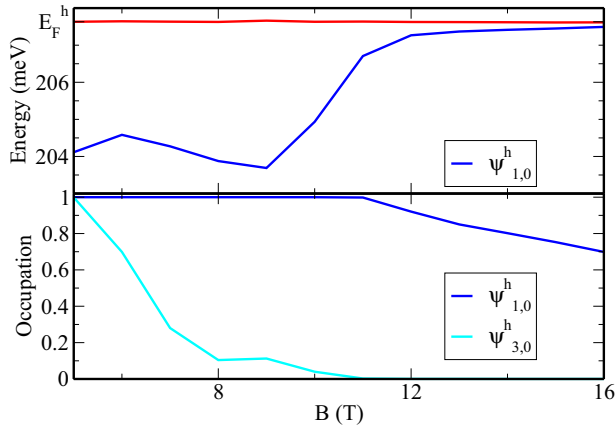
FIG. 4. (Color online) Energy and sub-band occupation for the sample of Fig. 2. Top: Energy of the ground hole state at $k = 0$ vs B. The horizontal line indicates the hole Fermi level. Bottom: Occupation of $n = 1$ (blue line) and $n = 3$ (cyan line) hole states at $k = 0$ as a function of the magnetic field.

holes with the same k. Hence, the overlap decreases and, as a consequence, the PL intensity decreases as well.

In the high-field regime, the emission energy of the e-h ground state increases linearly with the field, as expected [12]. The peak also reduces its intensity as a consequence of both the decrease of the overlap integral between hole and electron states (see Fig. 3) and the decreasing occupation of the electron ground state at $k = 0$.

At $n_1^{ph} = 10^6$ cm^{-1} the photoexcited hole density is of the same order as the free charge density (8.3×10^6 cm^{-1} at $B = 0$ T, 8.4×10^6 cm^{-1} at $B = 22$ T). Figure 5 displays the sub-band dispersion and the PL spectra for this configuration. The overall dispersion is similar to the previous case even though electrons now occupy a few excited sub-bands at the lowest field. The PL spectrum at $B = 0$ exhibits four peaks, with the one due to the e-h ground state at about 1520 meV being very

weak. Additional stronger peaks at 1523, 1526, and 1530 meV are due to transitions between excited states. All emission lines exhibit a diamagnetic shift at low fields and a linear one at high magnetic fields. At increasing fields, the number of emission lines decreases since the occupation of the upper electron levels vanishes. At $B = 10$ T only two peaks are visible, one related to the e-h ground state and the other one originating from the recombination of an electron in the ground state and a hole in the excited state ($n = 3$) spreading over the GaAs core (see the inset of the right panel of Fig. 5). As B increases, the $n = 3$ sub-band gets closer to the lowest one in the k interval around $k = 0$. This is due to the fact that the $n = 3$ hole state develops lobes localized on opposite sides of the structure where potential energy is lower with respect to the GaAs core. Therefore the two peaks approach each other and merge in a unique peak whose emission energy increases linearly with B.

In the large excitation power regime, namely, $n_1^{ph} = 10^7$ cm^{-1}, the density of photoexcited holes is about equal to free hole density (0.85×10^7 cm^{-1} at $B = 0$, 0.84×10^7 cm^{-1} at $B = 22$ T). Therefore, the electron density is now about one-half the total density of holes, and a large number of both conduction and valence sub-bands are occupied, as shown in Fig. 6. Consequently, the low-field PL spectrum shown in Fig. 6 is considerably more complex than in the previous cases, covering the range 1523 to 1555 meV. As B rises, the number of peaks decreases and in the high-field region three PL emission lines can be identified, each originating from *diagonal* transitions involving electron and hole states with $n = 1, 2, 3$ (the square modulus of these wave functions is reported in Fig. 7). Unlike the low excitation power regime, the ground hole state also spreads over the central region due to the Coulomb attraction from free electrons. The peak at 1545 meV for $B = 10$ T related to the transition $\psi_{3,0}^e \rightarrow \psi_{3,0}^h$ decreases its intensity with the field while the other two emission lines due to the $n = 1, 2$ diagonal transitions increase, unlike what was observed before in the PL spectra for lower excitation power. Here, the occupation number of $n = 1, 2$ electron and
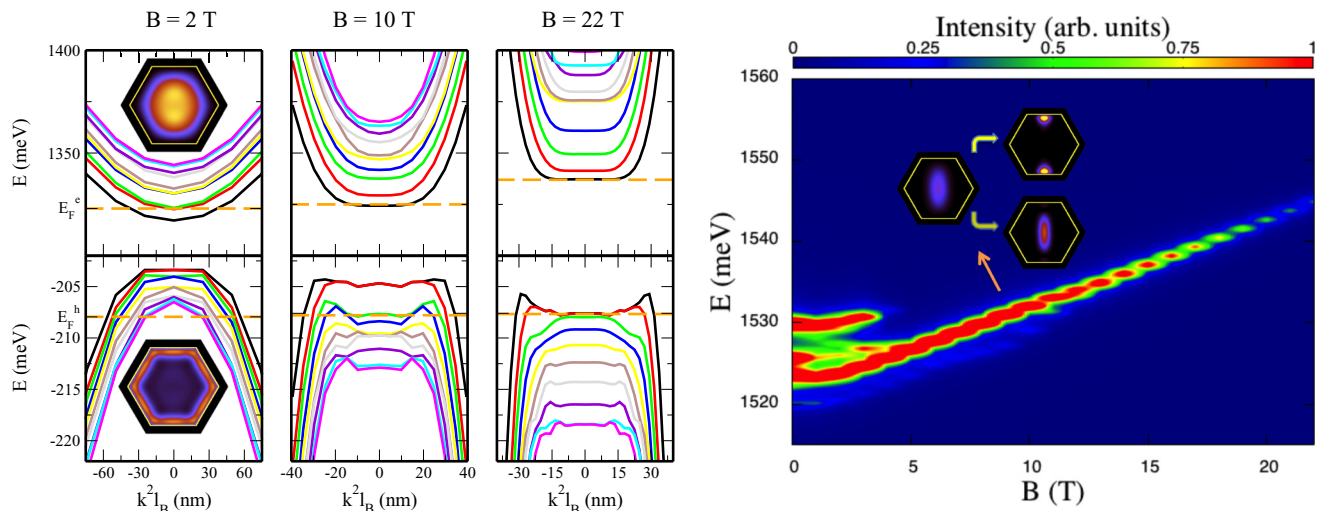

FIG. 5. (Color online) Same as Fig. 2, but with $n_1^{ph} = 10^6$ cm^{-1}. The inset in the right panel displays the squared envelope functions for the $n = 1$ electron (left) and $n = 1$ (top right) and $n = 3$ hole (bottom right) states whose recombinations yield the two peaks at $B = 10$ T.
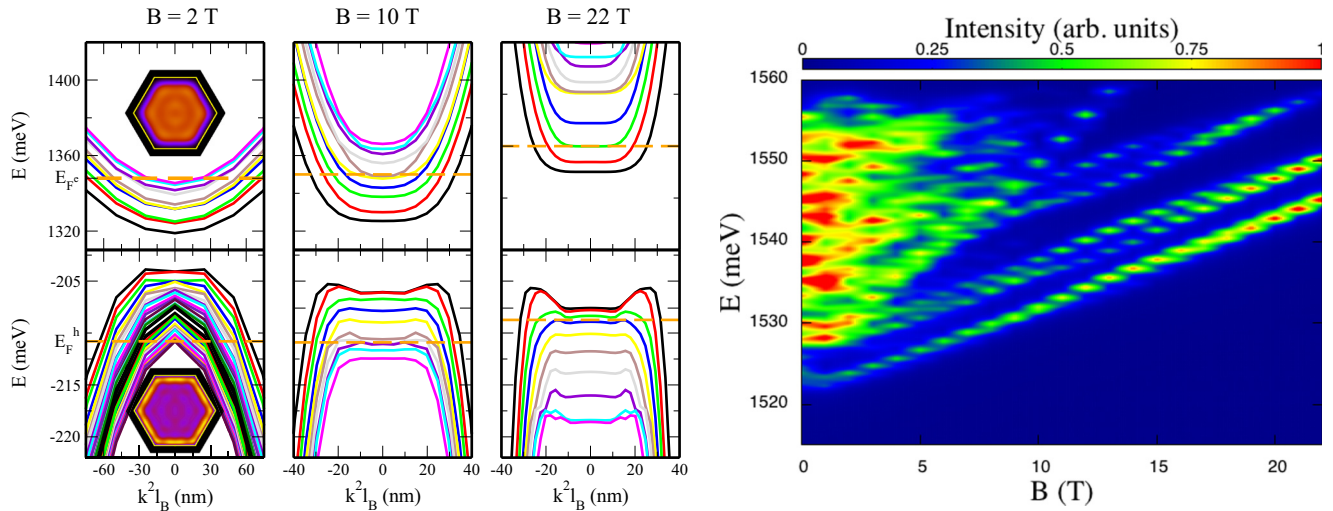
FIG. 6. (Color online) Same as Fig. 2, but with $n_1^{ph} = 10^7$ cm^{-1}.

hole levels at $k = 0$ is always equal to 1 for any value of B, and the intensity of the emission lines is only modulated by the overlap integral which increases at larger fields. The lowest electron and hole states exhibit the same localization: the ground states spread over the core while the $n = 2$ ones are concentrated in two lobes localized on opposite sides. Such features are more marked for larger fields and thus the integral overlap between the electron and holes states rises.

2. n doping

We next study the fan diagrams obtained in a n-doped sample with $n_D = 4.5 \times 10^{19}$ cm^{-3} and an $n_1^{ph} = 10^6$ cm^{-1} sample with the same field configuration as in the previous section. Now the hole density is only due to photoexcitation, while the electron density due to photoexcitation is small, but not negligible, with respect to the free charge induced by n doping (9.4×10^6 cm^{-1} at $B = 0$, 9.5×10^6 cm^{-1} at $B = 22$ T). From
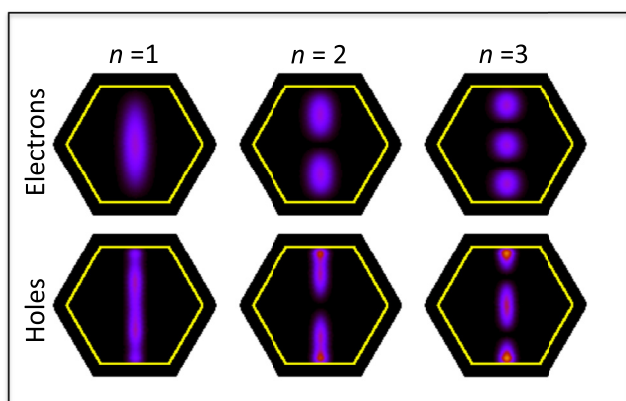

FIG. 7. (Color online) Square modulus of the lowest $k = 0$ electron (top) and hole (bottom) envelope function at $B = 22$ T for the sample of Fig. 6.

this point of view, this regime corresponds to the second case analyzed in p-doped systems (and reported in Fig. 5). Due to the large donor density, which induces an inversion layer at the heterointerface, in the n-doped case the electron sub-bands deviate significantly from parabolicity, while holes tend to form Landau-like and edge states. For sufficiently large fields, the electron sub-bands develop minima which correspond to states localized at the flanks.

The right panel of Fig. 8 displays the corresponding PL spectra. For $B = 0$ we observe several emission lines. Note that the lowest one is at 1515 meV, below the bulk GaAs band gap. Indeed, as shown in Fig. 9 (top panel), the hole ground state spreads over the GaAs core while the electron ground state is localized at the inner GaAs/AlAs interfaces depleting the central zone. The bending of the bands due to electrostatic potential mostly generated by the dopants is more pronounced in the regions farther away from the central core. Therefore, the down shift of electron levels is generally larger than for hole states, and, as a consequence, the energy of the ground e-h state lies below the bulk GaAs band gap. Such a behavior was not observed in the p-doping regime since in that case the band bending was less pronounced due to the smaller density of dopants ($n_A = 2.5 \times 10^{19}$ cm^{-3} versus $n_D = 4.5 \times 10^{19}$ cm^{-3}).

In this sample, the number of transitions at low fields is larger than for a p-doped sample in the corresponding regime of photoexcitation power, although the number of sub-bands occupied by the minority carriers is similar. This is due to the different localization of the majority charge which, for n-type doping (although mainly localized at the heterointerface, as seen in the bottom panel of Fig. 9), extends to the core and overlaps with the hole ground state. As the magnetic field increases, the number of emission lines decreases due to hole state depopulation. At $B = 10$ T, only the hole ground state and a few electron sub-bands are occupied while the Fermi level is pinned, as shown in the left panels of Fig. 8. In the intermediate-field regime we identify three main peaks originating from the recombination of the hole ground state with different electron levels.
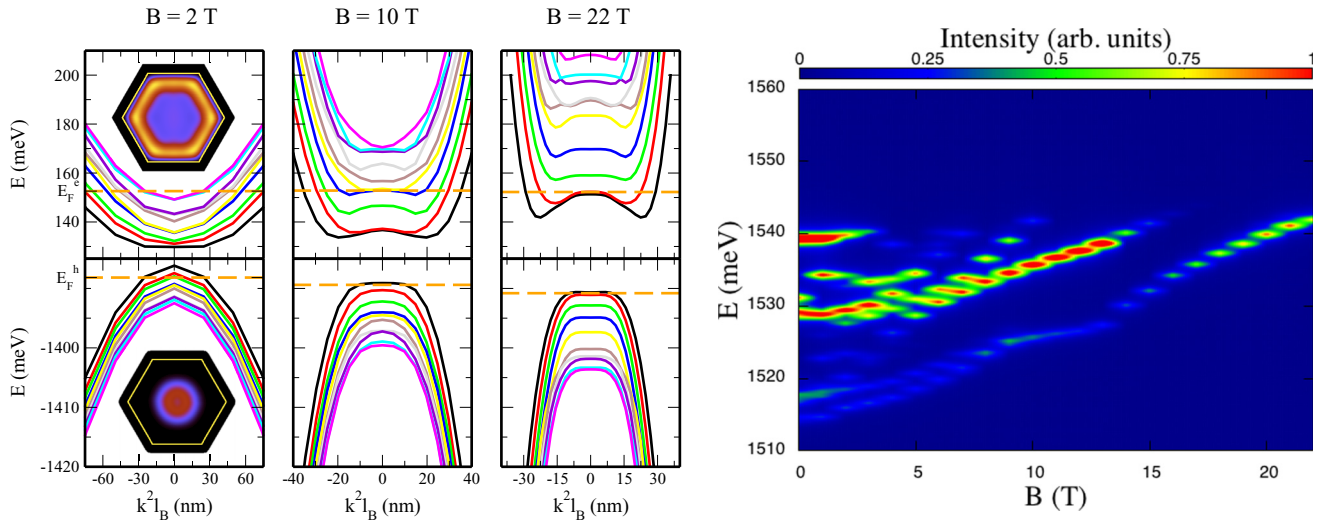
FIG. 8. (Color online) Same as in Fig. 2 but for a n-doped sample with $n_D = 4.5 \times 10^{19}$ and $n_1^{ph} = 10^6$ cm^{-1}.
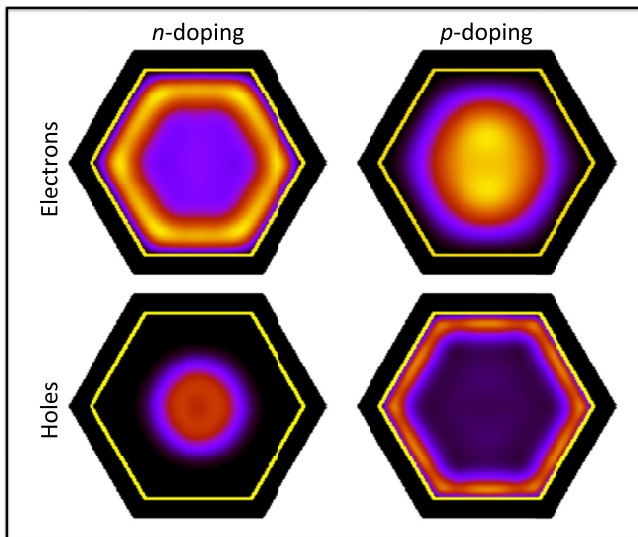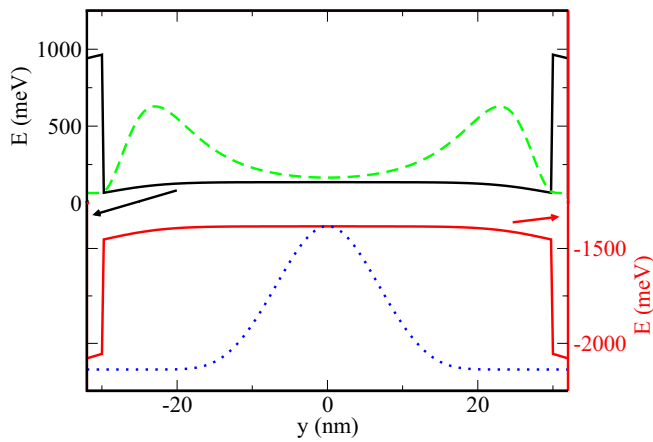

FIG. 9. (Color online) Top: Self-consistent conduction (black line) and valence (red line) band profile and the square modulus of the $n = 1$ electron (green dashed line) and hole (blue dotted line) wave function along the y axis at $B = 0$. Bottom: Electron and hole charge densities with $n_1^{Ph} = 10^6$ cm^{-1} at $B = 2$ T for $n_D = 4.5 \times 10^{19}$ cm^{-3} (left panels) and $n_A = 2.5 \times 10^{19}$ cm^{-3} (right panels).

The emission energy due to the e-h ground state exhibits a flat region between $B = 9$ and 12 T. For $B > 9$ T the occupation of the $n = 1$ hole state at $k = 0$ decreases significantly since the lowest sub-band flattens and states with $k \neq 0$ are increasingly populated at the expense of the $k = 0$ state, as shown in the top panels of Fig. 10. Since finite k states are localized away from the NW axis, the field induces a restructuring of the hole density which becomes anisotropic (see the bottom panel of Fig. 10).

For the high-field regime, only one peak survives, due to the recombination of the ground e-h state.

C. Anisotropy

Carriers are either homogeneously distributed around the heterointerface or form one-dimensional and 2D channels according to the device parameters. In the latter case, we
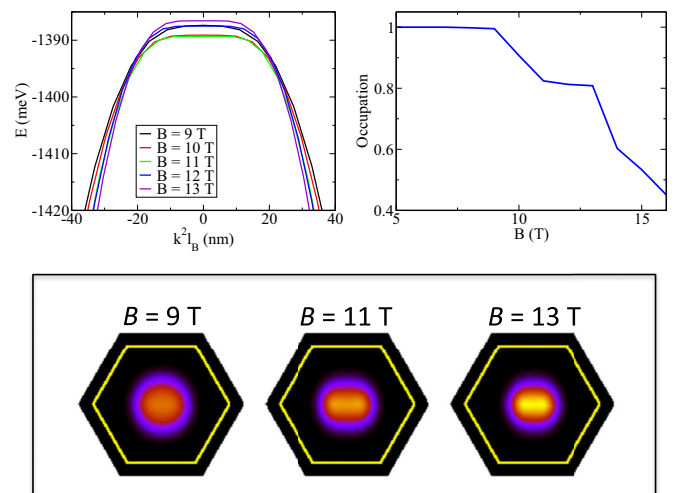

FIG. 10. (Color online) Top left: $n = 1$ hole sub-band vs kl_B^2 evaluated for B ranging from 9 to 13 T. Top right: Occupation of the $n = 1$ hole state at $k = 0$ vs B. Bottom: Hole gas density at selected fields, as indicated.
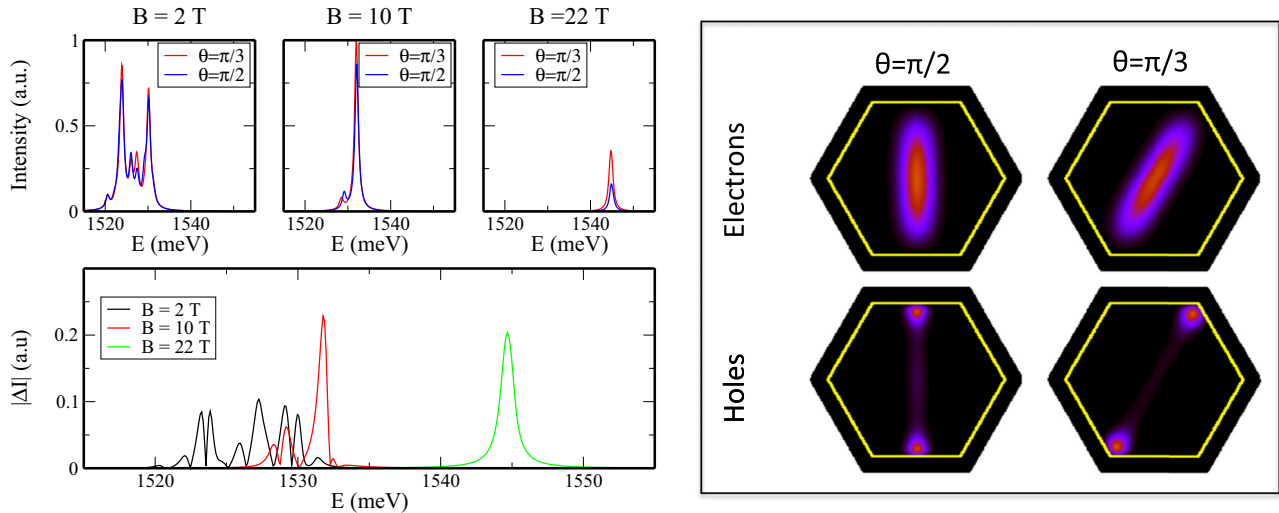
FIG. 11. (Color online) Left: PL spectra in different directions (top) and absolute difference between the PL spectra (bottom) at selected fields, as indicated. Right: Square modulus of the $n = 1$ hole and electron envelope functions at $k = 0$ and $B = 22$ T for the two field orientations.

expect the direction of the field to have a remarkable impact. Therefore, we next compare PL spectra with the field oriented in two nonequivalent directions, namely, perpendicular to the top/bottom facets ($\theta = \pi/2$) and along a maximal diameter ($\theta = \pi/3$). We assume p doping with $n_A = 2.5 \times 10^{19}$ cm^{-3} at the intermediate excitation power regime, that is, $n_1^{\text{Ph}} = 10^6$ cm^{-1}. The left panels of Fig. 11 display the PL spectra evaluated for the two configurations at different values of the field intensity.

The spectra exhibit the same qualitative behavior, with several emission lines at low B which reduce to one peak (ground e-h state) at larger fields. However, the emission intensity is anisotropic, especially at high-field intensity. At $B = 22$ T, the peak intensity at $\theta = \pi/3$ is about twice as strong as the one at $\theta = \pi/2$. This is due to the different localization of the $n = 1$ electron and hole states at $k = 0$, shown in the right panel of Fig. 11. The hole state shows two lobes localized by the strong carrier-carrier repulsion toward the bottom and top facets (at $\theta = \pi/2$) or corners (at $\theta = \pi/3$). Since the facet-to-facet distance is shorter, due to Coulomb interaction the energy of the state in the first configuration turns out to be a few tenths of meV greater than the one with the field along the maximal diameter. As a consequence, its occupation is smaller. The electron states elongate in the field direction and, also in this case, the energy level obtained at $\theta = \pi/2$ turns out to be greater than the one found at $\theta = \pi/3$, and this yields a discrepancy in the occupation of the states. Thus, the higher population of both $n = 1$ hole and electron states leads to the stronger intensity of the ground e-h state emission line at $\theta = \pi/3$ with respect to the one found at $\theta = \pi/2$.

IV. SUMMARY AND CONCLUSIONS

We have investigated theoretically the magneto-optical properties of hole and electron gases in the GaAs/AlAs core-multishell NWs which are either n- or p-doped and subject

to a transverse magnetic field. The tailoring of PL spectra by the field has been rationalized in different doping regimes. Calculations were performed by means of a self-consistent mean-field approach, with the inclusion of photogenerated hole-electron pairs that add to the free carriers induced by the modulation doping.

Our results indicate that the behavior of magneto-PL spectra offers a valuable guideline to estimate the density of the doping in CMS NWs. In fact, when the density of free carriers due to the doping is greater than the one of photogenerated charges, the spectra are quite simple and only the emission line due to the ground e-h state survives at high fields. Differently, when the excitation power is larger and the density of photoexcited carriers is comparable or higher with respect to the doping-induced free charge, several PL peaks are found that can be ascribed to recombinations from specific excited states, whose character is, in turn, strongly modified by the magnetic field.

We found a remarkable difference between samples with either electrons or holes as majority carriers. Indeed, at low magnetic fields and low photoexcitation power, the qualitative behavior of PL spectra for n- and p-doped samples is quite similar although, in the case of n doping, the number of emissions lines is greater than the one found for the p-doped sample. This is a consequence of the different localization pattern of the majority carriers. Still, in the low-field regime, when the density of photocreated hole-electron pairs is significant, the emission lines exhibit a diamagnetic shift, in both samples. This shift becomes linear for higher magnetic fields. However, the main peak, due to the ground e-h state, deviates from the expected behavior at low values of density of photogenerated hole-electron pairs. Specifically, in the intermediate-field regime, it exhibits a kink (p doping) or a flat region (n doping). In both cases this is due to the rearrangement of the gas of holes, whose heavier effective mass eases their localization near the interface with respect to the electrons. In the high power excitation

regime, the large Coulomb interaction prevents the hole gas rearrangement.

The differences in the magneto-PL spectra illustrated in this work are a valuable tool to discriminate not only the free-carrier density regime and type but also the relative density of doping- and photoexcitation-induced carriers. This, together with the assessment of the free-carrier spatial distribution, is pivotal in the characterization and engineering of CMS NWs.

[1] C. M. Lieber and Z. L. Wang, MRS Bull. **32**, 99 (2007).

[2] Y. Cui, Z. Zhong, D. Wang, W. U. Wang, and C. M. Lieber, Nano Lett. **3**, 149 (2003).

[3] J. A. Czaban, D. A. Thompson, and R. R. LaPierre, Nano Lett. **9**, 148 (2009).

[4] M. J. Holmes, K. Choi, S. Kako, M. Arita, and Y. Arakawa, Nano Lett. **14**, 982 (2014).

[5] F. Qian, S. Gradeak, Y. Li, C.-Y. Wen, and C. M. Lieber, Nano Lett. **5**, 2287 (2005).

[6] H. Shtrikman, R. Popovitz-Biro, A. Kretinin, and M. Heiblum, Nano Lett. **9**, 215 (2009).

[7] H. Shtrikman, R. Popovitz-Biro, A. Kretinin, L. Houben, M. Heiblum, M. Bukaa, M. Galicka, R. Buczko, and P. Kacman, Nano Lett. **9**, 1506 (2009).

[8] K. Tomioka, J. Motohisa, S. Hara, K. Hiruma, and T. Fukui, Nano Lett. **10**, 1639 (2010).

[9] M. J. Tambe, S. K. Lim, M. J. Smith, L. F. Allard, and S. Gradeak, Appl. Phys. Lett. **93**, 151917 (2008).

[10] S. Funk, M. Royo, I. Zardo, D. Rudolph, S. Morkötter, B. Mayer, J. Becker, A. Bechtold, S. Matich, M. Döblinger, M. Bichler, G. Koblmüller, J. J. Finley, A. Bertoni, G. Goldoni, and G. Abstreiter, Nano Lett. **13**, 6189 (2013).

[11] M. Fickenscher, T. Shi, H. E. Jackson, L. M. Smith, J. M. Yarrison-Rice, C. Zheng, P. Miller, J. Etheridge, B. M. Wong, Q. Gao, S. Deshpande, H. H. Tan, and C. Jagadish, Nano Lett. **13**, 1016 (2013).

[12] J. Jadczak, P. Plochocka, A. Mitioglu, I. Breslavetz, M. Royo, A. Bertoni, G. Goldoni, T. Smolenski, P. Kossacki, A. Kretinin, H. Shtrikman, and D. K. Maude, Nano Lett. **14**, 2807 (2014).

[13] T. Shi, H. E. Jackson, L. M. Smith, N. Jiang, Q. Gao, H. H. Tan, C. Jagadish, C. Zheng, and J. Etheridge, Nano Lett. **15**, 1876 (2015).

[14] B. M. Wong, F. Léonard, Q. Li, and G. T. Wang, Nano Lett. **11**, 3074 (2011).

[15] A. Bertoni, M. Royo, F. Mahawish, and G. Goldoni, Phys. Rev. B **84**, 205323 (2011).

[16] K. Tomioka, M. Yoshimura, and T. Fukui, Nature (London) **488**, 189 (2012).

[17] H. Ajiki and T. Ando, J. Phys. Soc. Jpn. **62**, 1255 (1993).

[18] G. Ferrari, A. Bertoni, G. Goldoni, and E. Molinari, Phys. Rev. B **78**, 115326 (2008).

[19] S. Bellucci and P. Onorato, Phys. Rev. B **82**, 205305 (2010).

[20] G. Ferrari, G. Goldoni, A. Bertoni, G. Cuoghi, and E. Molinari, Nano Lett. **9**, 1631 (2009).

[21] M. Royo, A. Bertoni, and G. Goldoni, Phys. Rev. B **87**, 115316 (2013).

[22] M. Royo, C. Segarra, A. Bertoni, G. Goldoni, and J. Planelles, Phys. Rev. B **91**, 115440 (2015).

[23] L. V. Titova, T. B. Hoang, J. M. Yarrison-Rice, H. E. Jackson, Y. Kim, H. J. Joyce, Q. Gao, H. H. Tan, C. Jagadish, X. Zhang, J. Zou, and L. M. Smith, Nano Lett. **7**, 3383 (2007).

[24] T. B. Hoang, L. V. Titova, J. M. Yarrison-Rice, H. E. Jackson, A. O. Govorov, Y. Kim, H. J. Joyce, H. H. Tan, C. Jagadish, and L. M. Smith, Nano Lett. **7**, 588 (2007).

[25] J. L. Boland, S. Conesa-Boj, P. Parkinson, G. Tütüncüoglu, F. Matteini, D. Rüffer, A. Casadei, F. Amaduzzi, F. Jabeen, C. L. Davies, H. J. Joyce, L. M. Herz, A. Fontcuberta i Morral, and M. B. Johnston, Nano Lett. **15**, 1336 (2015).

[26] L. M. Smith, H. E. Jackson, J. M. Yarrison-Rice, and C. Jagadish, Semicond. Sci. Technol. **25**, 024010 (2010).

[27] P. Plochocka, A. A. Mitioglu, D. K. Maude, G. L. J. A. Rikken, A. Granados del guila, P. C. M. Christianen, P. Kacman, and H. Shtrikman, Nano Lett. **13**, 2442 (2013).

[28] The small Zeeman energy (<0.3 meV at the largest field used) is below the thermal linewidth [12] and has been neglected.

[29] F. Rossi and E. Molinari, Phys. Rev. Lett. **76**, 3642 (1996).

[30] S. Sedlmaier, M. Stopa, G. Schedelbeck, W. Wegscheider, and G. Abstreiter, Phys. Rev. B **65**, 201304 (2002).

[31] We do not include the exchange and correlations effects in the mean field since they turn out to be negligible [39,15,14].

[32] Due to the symmetry of the Hamiltonian in Eq. (2), states with negative k can be obtained from $(\mathbf{r},k) \to (-\mathbf{r}, -k)$.

[33] G. Bastard, *Wave Mechanics Applied to Semiconductor Heterostructures*, Monographies de Physique (Les Éditions de Physique, New York, 1988).

[34] M. D. Pashley, K. W. Haberern, R. M. Feenstra, and P. D. Kirchner, Phys. Rev. B **48**, 4612 (1993).

[35] M. Levinshtein, S. Rumyantsev, and M. Shur, *Handbook Series on Semiconductor Parameters* (World Scientific, Singapore, 1996).

[36] G. Fishman, Phys. Rev. B **52**, 11132 (1995).

[37] G. Goldoni, F. Rossi, E. Molinari, and A. Fasolino, Phys. Rev. B **55**, 7110 (1997).

[38] P. YU and M. Cardona, *Fundamentals of Semiconductors: Physics and Materials Properties* (Springer, New York, 2013).

[39] B. Jogai, J. Appl. Phys. **91**, 3721 (2002).